Finite-Area Membrane Metasurfaces for Enhancing Light-Matter Coupling in Monolayer Transition Metal Dichalcogenides

Journal:	*ACS Nano*
Manuscript ID	nn-2024-055605.R2
Manuscript Type:	Article
Date Submitted by the Author:	n/a
Complete List of Authors:	Ho, Ya-Lun; National Institute for Materials Science Fong, Chee Fai; RIKEN Cluster for Pioneering Research, Nanoscale Quantum Photonics Laboratory Wu, YenJu; National Institute for Materials Science, Konishi, Kuniaki; The University of Tokyo, Institute for Photon Science and Technology Deng, Chih-Zong; The University of Tokyo Fu, Jui-Han; The University of Tokyo Kato, Yuichiro; RIKEN, Nanoscale Quantum Photonics Laboratory Tsukagoshi, Kazuhito; National Institute for Materials Science , MANA Tung, Vincent; The University of Tokyo; King Abdullah University of Science and Technology Chen, Chun-Wei; National Taiwan University, Materials Science and Engineering

Finite-Area Membrane Metasurfaces for Enhancing Light-Matter Coupling in Monolayer Transition Metal Dichalcogenides

Ya-Lun Ho[1], Chee Fai Fong[2], Yen-Ju Wu[3], Kuniaki Konishi[4], Chih-Zong Deng[4], Jui-Han Fu[5], Yuichiro K. Kato[2,6], Kazuhito Tsukagoshi[7], Vincent Tung[5], and Chun-Wei Chen[8,9]*

[1]Research Center for Electronic and Optical Materials, National Institute for Materials Science (NIMS), 1-1 Namiki, Tsukuba, Ibaraki 305-0044, Japan

[2]Nanoscale Quantum Photonics Laboratory, RIKEN Cluster for Pioneering Research, 2-1 Hirosawa, Wako, Saitama 351-0198, Japan

[3]Center for Basic Research on Materials, National Institute for Materials Science (NIMS), 1-2-1 Sengen, Tsukuba, Ibaraki 305-0047, Japan

[4]Institute for Photon Science and Technology, The University of Tokyo, 7-3-1 Hongo, Bunkyo, Tokyo 113-0033, Japan

[5]Department of Chemical System Engineering, School of Engineering, The University of Tokyo, 7-3-1 Hongo, Bunkyo, Tokyo 113-8656, Japan

[6]Quantum Optoelectronics Research Team, RIKEN Center for Advanced Photonics, 2-1
Hirosawa, Wako, Saitama 351-0198, Japan

[7]Research Center for Materials Nanoarchitectonics (MANA), National Institute for Materials
Science (NIMS), 1-1 Namiki, Tsukuba, Ibaraki 305-0044, Japan

[8]Department of Materials Science and Engineering, National Taiwan University, No. 1, Sec. 4,
Roosevelt Rd., Taipei 10617, Taiwan

[9]Center of Atomic Initiative for New Materials (AI-MAT), National Taiwan University, No. 1,
Sec. 4, Roosevelt Rd., Taipei 10617, Taiwan

ABSTRACT.

Transition metal dichalcogenides (TMDCs) are at the forefront of nanophotonics because of their exceptional optical characteristics. The 2D architecture of TMDCs facilitates efficient light absorption and emission, holding tantalizing potential for next-generation nanophotonic and quantum devices. Yet, the atomic thinness limits their interaction volume with light, affecting light-matter interaction and quantum efficiency. The light coupling in the 2D layered TMDCs can be enhanced by integration with photonic structure, and the metasurfaces supporting bound states in the continuum (BICs) offer strong confinement of optical fields, ideal for coupling with 2D TMDCs. Here, we demonstrate enhanced light-matter coupling by integrating TMDC monolayers, including WSe_2 and MoS_2, with a finite-area membrane metasurface, leading to amplified and high-quality-factor (Q-factor) spontaneous emission from quasi-BIC-coupled TMDC monolayers.

The high-Q-factor emission extends over an area with a scale of a few micrometers while maintaining the high-Q factor across the emission area. Notably, the suspended finite-area membrane metasurface, which is freestanding in air rather than positioned atop a substrate, minimizes radiation loss while enhancing light-matter interaction in the TMDC monolayer. Furthermore, the predominantly in-plane dipole orientation of excitons within TMDC monolayers results in distinctive enhancement behaviors for emission, contingent on the excitation power, when coupled with quasi-BIC modes exhibiting TE and TM resonances. This work introduces a nanophotonic platform for robust coupling of membrane metasurfaces with 2D materials, offering possibilities for developing 2D material-based nanophotonic and quantum devices.

KEYWORDS.

Suspended metasurface, Membranes, BIC, Light-matter coupling, TMDC monolayers, WSe_2, MoS_2

TEXT.

Van der Waals layered materials such as graphene, hexagonal boron nitride (hBN), and transition metal dichalcogenides (TMDCs) are generating excitement in the field of nanophotonics.[1, 2] Semiconducting TMDCs have a direct bandgap at monolayer and bright optical emission,[3, 4] as well as reduced Coulomb screening, which result in strongly Coulomb-bound electron-hole pairs, known as excitons.[5, 6] Due to the high exciton binding energies (> 200 meV), the TMDCs' optical properties hinge on their excitonic responses even up to room temperature.[7-9] Despite these favorable properties, the atomic thickness of TMDCs limits their interaction volume with light, weakening light-matter interaction.[10] Their 2D nature also increases the nonradiative exciton-exciton annihilation, reducing quantum efficiency. To create practical devices, TMDCs can be heterogeneously integrated with different target substrates, including nanophotonic architectures, such as photonic-crystal cavities, plasmonic nanostructures, and dielectric metasurfaces, to engineer the environment experienced by the 2D excitons for enhanced light-matter coupling.[11-16]

Photonic bound states in the continuum (BICs) represent an optical phenomenon characterized by the confinement of optical modes within the radiative continuum but do not couple to the radiative field in free space.[17-19] An ideal BIC confines optical fields spatially and spectrally for an indefinite amount of time with no energy dissipation, thus exhibiting an infinite Q factor. The non-coupling of the mode to the radiative field arises from the symmetry mismatch between the near field and the far field (destruction interference in the near field or the far field). In practice, the conditions for a BIC are usually not fully met, leading to a so-called quasi-BIC, which is an imperfectly confined BIC that could couple to the radiative continuum. This enables quasi-BIC to be excited by external fields and used as a platform for light-matter coupling.[20-26] Nanophotonic structures with BICs are usually implemented on planar surfaces, making them inherently compatible with 2D layered materials. This compatibility is particularly significant in the case of optically active TMDC monolayers, which not only enhances the confinement of light within the vicinity of the TMDC but also provides a means to tailor and manipulate the optical properties of 2D materials at the atomic scale. In recent years, the coupling of BIC modes with TMDC monolayers has demonstrated remarkable potential across various optical and quantum technologies.[27-31]

Managing radiation loss in BICs is critically important and intimately associated with the symmetrical attributes of the out-of-plane orientation within the photonic architecture.[32, 33] Out-of-plane symmetry prevents the coupling of BICs to radiative modes, confining optical energy within the structure and minimizing the potential for radiation leakage. This symmetry-induced suppression of radiation loss is a critical factor in the optical properties of BICs, enhancing light-matter interaction within the confined region. However, it is worth noting that achieving perfect symmetry or maintaining it in the presence of imperfections can pose challenges in the experimental realization of BICs. To date, most of the photonic structures supporting BICs for 2D material-coupling consist of periodic structures sitting in/on a substrate. This underlying substrate significantly facilitates the break of out-of-plane symmetry and leakage of fields, leading to reduced confinement of the BIC and, thus, weaker light-matter coupling with the integrated 2D materials. Utilizing a membrane as the substrate for BIC photonic structures offers a key benefit by reducing substrate leakage. Membrane photonic structures supporting BIC modes have been demonstrated,[34-38] and it is highly desired to further demonstrate the membrane photonic structure supporting BIC modes in coupling with TMDC monolayers.[39] This step is essential for expanding the scope of applications, marking a significant advancement in integrating BIC photonic structures with 2D materials.

In this work, we demonstrate the enhanced light-matter coupling by integrating TMDC monolayers, including WSe_2 and MoS_2, with a finite-area suspended membrane metasurface, presenting the concentrated spontaneous emission from quasi-BIC coupled TMDC monolayer (Figure 1). The freestanding membrane structure in air, rather than positioned atop a substrate, is presented, leading to improved optical confinement and amplified field intensity in the quasi-BIC mode. Based on the quasi-BIC mode in the finite-area silicon nitride (SiN) membrane metasurface, the spontaneous emission with sizes in the range of a few micrometers, accompanied by a high Q factor of up to 6800 in visible, is observed. The emission behavior resulting from the quasi-BIC mode diverges notably from that of optical guided modes, which show a low Q factor and weak emission. By coupling TMDC monolayers to the finite-area membrane metasurface, enhanced emission from quasi-BIC-coupled TMDC monolayers with a Q factor reaching up to 2800 is measured. The high-Q emission extends over an area of a few micrometers while maintaining the high-Q factor across the entire emission region. This behavior differs significantly from the emission characteristics of photonic-crystal cavities, plasmonic nanostructures, and dielectric nanoantenna structures.[11,16,40-45] By analyzing the excitation power dependence on the TMDC-coupled metasurface membrane, it is determined that spontaneous emission experiences a more significant enhancement when coupled to the quasi-BIC modes relative to the guided modes. This suggests efficient coupling between the emitter surface and the metasurface cavity, demonstrating the advantage of the membrane metasurface for 2D layered materials. Furthermore, since the excitons within the TMDC monolayer primarily exhibit an in-plane dipole orientation, the quasi-BIC modes with TE and

TM resonance present significantly different enhancement behaviors of emission with excitation power. Our study not only explores the surface emission characteristics of the quasi-BIC mode in finite-area metasurfaces but also introduces a nanophotonic platform for the robust coupling of the membrane metasurface with 2D materials. These findings emphasize the crucial role of membrane design in shaping nanophotonic metasurfaces that support BIC, offering possibilities for developing 2D material-based nanophotonic and quantum devices.

Results and Discussion

Design and characterization of optical guided modes and quasi-BIC modes based on membrane metasurfaces

The membrane metasurface consists of a triangular lattice of airholes with lattice period, *a,* and radius, *r* in a SiN slab of thickness, *t* (Figure 2a). To optimize the design of the metasurface, we first perform numerical rigorous coupled-wave analysis (RCWA) for a structure with the following parameters, $a = 400$ nm, $r = 90$ nm, and $t = 205$ nm. Further simulation details are provided in the Methods section. By varying the incident angles of *x*-polarized excitation light along the *x*- and *y*-axes (θ_x and θ_y), we can simulate the reflectance spectra (dispersion diagrams) along the *x*- and *y*-directions as presented in Figure 2a and 2b. The incident angle is kept between 0° and 5° in order to focus on the symmetry-protected BICs that are expected to arise near 0° (i.e., Γ point). Various resonances are identified, with slight but notable differences between the dispersion diagrams along the *x*- and *y*-directions. The transverse electric (TE) and transverse magnetic (TM) natures of the mode can be determined by looking at the profile of the field components (see Figure S1 for further details). The two resonances appearing to the shorter wavelength side of 550 nm in the dispersion diagrams are optical guided modes. In contrast, the resonances above 550 nm are attributed to BICs with their vanishing intensity at 0˚. The assignments of the modes are further corroborated by the variations of the Q factor of the resonances, as shown in Figure 2c and 2d. The guided modes exhibit a consistently low Q factor on the order of 10^1-10^2, regardless of the angle. The BIC resonances, on the other hand, exhibit Q factors that approach infinity with a decreased angle.[17-19,46]

Figure 2e and 2f display the distributions of electric energy density for the resonances at 2˚. The guided modes depicted in the *x*- and *y*-dispersion diagrams correspond to identical modes (TE_{guided} mode and TM_{guided} mode, see Figure S1), as evidenced by their matching electric energy density distributions. The TE_{guided} mode exhibits electric field distribution in the air holes and the areas between the holes, reaching an electric energy density of the order of 10^1, whereas the TM_{guided} mode displays a stronger electric energy density of the order of 10^2 with a dipolar distribution at the edge of the air holes. Narrowband resonances around 560 nm are noticeable in both the *x*-direction and *y*-direction dispersion diagrams, exhibiting a redshift trend as the incident angle increases. The simulated Q factors increase as the angle decreases, approaching 10^7, indicative of the BIC modes ($TM_{BIC,x}$ and $TM_{BIC,y}$ mode, see Figure S1) within the membrane metasurface. It is noted that the minimum angle in the simulation is set to 0.05˚, imposing limitations on the Q factor as it approaches 0˚. In $TM_{BIC,x}$ and $TM_{BIC,y}$, resonances exhibit intensive electric field enhancement in between air holes along the *x*- and *y*-direction aligning with the angle directions, indicating closely resonant wavelengths at a small angle. The electric energy densities of $\mathrm{TM}_{\mathrm{BIC},x}$ and $\mathrm{TM}_{\mathrm{BIC},y}$ modes reach up to the order of 10^4, a significantly stronger value than that of the guided mode. In the *y*-direction dispersion diagram, another BIC mode at approximately 565 nm, $\mathrm{TE}_{\mathrm{BIC},y}$ mode, exhibits electric field enhancement surrounding the air hole with a relatively lower magnitude, on the order of 10^2-10^3, and lower Q factors in comparison to $\mathrm{TM}_{\mathrm{BIC},y}$ mode. Another BIC mode observed in the *x*-direction dispersion is identified around 573 nm as $\mathrm{TE}_{\mathrm{BIC},x}$ mode. Among all the modes observed in the dispersion diagram within the region of interest, the $\mathrm{TE}_{\mathrm{BIC},y2}$ mode at 584 nm, in the dispersion along the *y*-axis, exhibits the largest electric energy density above the order of 10^4 along with high Q factors.

To compare the simulated resonances with those observed under actual experimental conditions, we conducted additional finite-difference time-domain (FDTD) simulations on finite-area structures comparable in scale to those used in the experiments. Simulation details are provided in the Methods section. Figure 3 presents the distributions of electric energy density for the resonances of the $\mathrm{TE}_{\mathrm{guided}}$ mode (Figure 3a) and $\mathrm{TE}_{\mathrm{BIC},y2}$ mode (Figure 3b) in the finite-area membrane metasurface for representative cases. Both the guided and quasi-BIC mode profiles show a similar distribution to those in the infinite case, indicating that these are indeed essentially the same modes regardless of system size. Despite the finite size of the membrane metasurface, we could gain insights into its optical properties by analyzing the infinite system, i.e., by studying the field distribution in a unit cell with periodic boundary conditions, since the same quasi-BIC and guided modes of interest are present in both the finite and infinite cases. From the simulated mode profiles of the finite-size membrane, the results indicate that the $\mathrm{TE}_{\mathrm{guided}}$ mode exhibits a relatively homogeneous distribution across the entire metasurface area, with energy leakage observed from the metasurface edges in both *x* and *y* directions. Conversely, the $TE_{BIC,y2}$ mode shows an obvious concentration of electric energy density at the center of the metasurface. The distribution near the center closely resembles the pattern observed in the simulation of the periodic structure modeled as an infinite lattice. However, away from the center, the distribution becomes asymmetric within each unit cell and shows a lower intensity compared to the central region. This analysis suggests the differences in the spatial distribution of electric energy density between the guided and quasi-BIC modes, emphasizing the effectiveness of the finite-area metasurface design in achieving high-Q resonances with spatially localized energy confinement.[47]

Furthermore, to highlight the importance of using an air-suspended membrane, we present a comparative analysis between the membrane metasurface and a metasurface located on top of a SiO_2 substrate. The reflectance spectra at 2° of the membrane metasurface and the substrate-based metasurface are shown in Figure 4a. The simulation parameters remain the same as that in Figure 2. In the case of the substrate-based metasurface, identical resonances appear in the spectra, with the resonances showing a general redshift compared to those in the membrane metasurface due to the increased effective refractive index of the structure. We will focus our discussion here by comparing the TE_{guided} and $TE_{BIC,y2}$ modes in the two cases. For the TE_{guided} mode, the electric energy density (Figure 4b) remains almost unchanged in both membrane and substrate-based metasurfaces. However, for the $TE_{BIC,y2}$ mode, the intensity of the electric energy density distribution (Figure 4c) in the membrane metasurface is 2.7 times higher than that in the substrate-based metasurface. Additionally, the electric field distributions in the *z*-direction (E_z)

for the $\mathrm{TE}_{\mathrm{BIC},y2}$ mode show a significant difference between the membrane metasurface and the substrate-based metasurface. In the membrane metasurface, the E_z field distribution for the $\mathrm{TE}_{\mathrm{BIC},y2}$ mode exhibits a nearly symmetrical pattern, whereas in the substrate-based metasurface, the $\mathrm{TE}_{\mathrm{BIC},y2}$ mode shows an asymmetrical E_z distribution. These results suggest that preserving out-of-plane symmetry promotes significant field confinement of BIC modes, highlighting the important role of membrane metasurface design in achieving highly confined modes.

Enhanced spontaneous emission and emission intensity distribution from the finite-area membrane metasurface

Next, we performed optical characterization of the finite-area membrane metasurface. The SEM images of the membrane metasurface sample are shown in Figure S2. Comprehensive details of the optical measurements are provided in the Method section. The spontaneous emission spectrum from the finite-area SiN membrane metasurface is shown in Figure 5a unveiling multiple metasurface enhanced emission peaks. Two emission peaks on the shorter wavelength side of the spectrum denoted as P_A and P_B exhibit broad linewidths and relatively low peak intensities that correspond to the guided modes $\mathrm{TE}_{\mathrm{guided}}$ and $\mathrm{TM}_{\mathrm{guided}}$, respectively. The Q factor of the emission peak at P_B is ~ 300. In the wavelength range between 560 nm and 580 nm, four resolved peaks can be observed (Figure 5b) with P_C exhibiting high peak intensity and a narrow linewidth corresponding to Q ~ 3300. Another emission peak P_G appears at approximately 598 nm (Figure 5c) displaying the narrowest linewidth with a Q factor approaching 6800 (limited by spectrometer resolution), which is notably high for photonic structures in the visible region.

These five peaks P_C - P_G are associated with the $TM_{BIC,x}$, $TM_{BIC,y}$, $TE_{BIC,y}$, $TE_{BIC,x}$, and $TE_{BIC,y2}$ modes in the simulation from Figure 2a. Given the finite size of the metasurface, the quasi-BIC modes exhibit as observable peaks with finite linewidths in the emission spectrum. It is important to note that the emission spectrum was measured with an objective lens of NA = 0.25. Since the BIC resonances exhibit wavelength shifts with emission angle, the emission peaks in the resulting emission spectrum are expected to have broadened linewidths, suggesting that these peaks could have even higher intrinsic Q factors.

We further performed 2D surface emission imaging to investigate the spatial distribution of the emission intensity of guided modes and quasi-BIC modes (Figure 5d). The guided modes P_A and P_B exhibit a relatively homogeneous emission throughout the finite area of the membrane metasurface. In contrast, the quasi-BIC modes exhibit more varied and complex distributions. Emissions from P_C, P_D, and P_G are significantly concentrated at the center of the metasurface, whereas P_E and P_F show more diffused emission distributions. The differences in the distribution profiles between the guided and quasi-BIC modes reflect the underlying optical confinement mechanisms. The optical guided modes arise from total internal reflection within the metasurface, in contrast to the quasi-BIC modes which originate from the symmetry-mismatch of the near field and far field profiles. Near the boundaries, the broken symmetry renders the metasurface incapable of robustly supporting quasi-BIC modes, causing the emission from the modes to be more intense in regions away from the boundaries. The properties of the near field profile such as field symmetry, field amplitude and phase profile, as well as the k-momentum components govern the coupling of the quasi-BIC modes to the radiative modes, giving rise to the variations in the 2D emission spatial distribution. Furthermore, the emission distribution correlates with the Q factors: concentrated emission corresponds to high Q factors, while dispersed emission corresponds to low Q factors.

In addition, since the symmetry-protected quasi-BIC modes occur at the Γ point, their emitted light maintains high directionality. In Figure S3, the spontaneous emission spectra of the quasi-BIC modes, measured under objective lenses with 10x (NA = 0.25) and 20x (NA = 0.45) magnifications, reveal emission peaks corresponding to the same quasi-BIC modes, exhibiting identical linewidths. This result suggests that the emission occurs within a narrowly confined angle in the normal direction.

Regarding the membrane metasurface, the resonant wavelengths of the quasi-BIC modes can be tuned by varying the dimensions of the metasurface structure (see Figure S4). The spontaneous emission spectra from the membrane metasurface, featuring lattice periods of 500 nm and 600 nm, are presented in Figure S5a, showing the presence of both guided modes and quasi-BIC modes. In Figure S5b, the emission spectrum from the SiN membrane without the metasurface structure is compared with that of the membrane metasurface with the periods of 600 nm, accompanied by an illustration of the enhancement factor between the non-structured membrane and the metasurface. The emission enhancement factor is significantly higher for the quasi-BIC mode resonances compared to the guided mode resonances. This observation is consistent with the simulated electric energy density distribution depicted in Figure 2e and 2f, reinforcing the correlation between the enhancement factor and the strong electric field characteristics associated with the quasi-BIC modes.

Coupling TMDC monolayers to the membrane metasurface through quasi-BIC modes

To demonstrate the coupling between the TMDC monolayer and the membrane metasurface, we integrate WSe_2 and MoS_2 monolayer onto the membrane metasurface by the dry transfer technique (see the Methods section for further details). Since the WSe_2 monolayer exhibits a strong spontaneous emission centered at 750 nm, the WSe_2 monolayer flake is transferred onto a membrane metasurface with $a = 600$ nm which supports quasi-BIC modes near the emission band of the WSe_2 monolayer (see Figure S5a). Figure 6 shows the emission spectra of the membrane metasurface with and without the WSe_2 monolayer. The guided and quasi-BIC resonances are redshifted in the case of the membrane metasurface with the WSe_2 monolayer due to the increase in the effective refractive index. The emission from the WSe_2 monolayer spectrally overlaps with the quasi-BIC modes resulting in a clear emission enhancement, reaching almost 40 times the intensity when compared to emission from the WSe_2 monolayer on the bare membrane (see the inset in Figure 6).

We performed excitation power dependence measurement to further investigate the light-matter interaction properties between the WSe_2 monolayer and the quasi-BIC modes of the membrane metasurface. Figure 7a and 7b summarize the emission spectra of the metasurface without and with the WSe_2 monolayer, respectively, measured under various excitation powers ranging from 0.1 mW to 5 mW. The spatial distribution of the spontaneous emission is presented in Figure 7d, allowing us to identify the corresponding guided and quasi-BIC modes. The emission intensity normalized to that at 0.1 mW excitation power of each guided mode and quasi-BIC mode is shown in the insets of each plot. Without the WSe_2 monolayer on the membrane metasurface, both guided and quasi-BIC modes demonstrate a consistent increase in the emission intensity with excitation power, displaying identical slopes. However, the power dependence of emission intensity of the WSe_2 monolayer coupled to the quasi-BIC modes in the membrane metasurface exhibits a larger slope than that of the guided modes. The larger slope can be attributed to the stronger electric energy density of the quasi-BIC modes, which is associated with a more significant optical density of states and thus leads to a more prominent Purcell enhancement of the emission from the WSe_2 monolayer. In addition, the coupling of the WSe_2 monolayer emission to different quasi-BIC modes also exhibits varying dependences on the excitation power. The intensity of $P_{C'}$ and $P_{D'}$ shows a noticeable saturation behavior with excitation power. This saturation can be attributed to the localization of the emission of $P_{C'}$ and $P_{D'}$ in a small central region of the membrane metasurface. When coupled with the WSe_2 monolayer, the rapid increase in carrier density in this localized area may lead to non-radiative exciton-exciton annihilation,[48] resulting in the observed saturation of emission intensity. Moreover, the relatively low intensity at saturation of $P_{C'}$ and $P_{D'}$ is due to its TM mode nature. Excitons within the WSe_2 monolayer primarily exhibit an in-plane dipole orientation, leading to relatively weak coupling with the TM quasi-BIC modes that predominantly feature E_z field components. On the other hand, the WSe_2 monolayer emission coupled to $P_{E'}$ and $P_{F'}$, which are

TE polarized, shows a more significant enhancement of spontaneous emission with excitation power.

It is noted that although the Q factors of emission peaks from the WSe_2 monolayer coupled to the quasi-BIC modes in the membrane metasurface at 750-780 nm are difficult to clarify due to the overlap of the modes, an emission peak at 814 is observed and achieves a Q factor of 2800 (Figure 7c). This high-Q emission ($P_{G'}$) extends over an area with a diameter of 5 μm while maintaining the high-Q factor across the entire emission area, as shown in Figure 7d and S6. The TMDC monolayers coupled to the finite-area membrane metasurface supporting quasi-BIC reveal significant differences in their emission characteristics compared to other nanophotonic platforms. The TMDC monolayers coupled to photonic-crystal cavities[11,40-42] feature emission Q factors on a comparable scale to that of the quasi-BIC metasurface demonstrated in this work. However, the emission area in photonic-crystal cavities is typically confined to sub-micrometer scales. Conversely, TMDC monolayers coupled to photonic-crystal waveguide structures[40,43] exhibit low Q factors, with the emission area extending to tens to hundreds of micrometers. This indicates the formation of guided modes with larger interaction areas. When TMDC monolayers are coupled to plasmonic nanostructures,[44,45] there is a significant enhancement of emission within highly localized regions (below 100 nm) with no substantial change in the Q factor compared to the emissions from TMDC monolayers without coupling to the structures. In summary, the coupling of TMDC monolayers to quasi-BIC mode-supported membrane metasurfaces results in high-Q factor emissions, comparable to those achieved with photonic-crystal cavities, while also extending the emission area to several micrometers.

Furthermore, the emission from the MoS_2 monolayer coupled to the membrane metasurface with the lattice period of 500 nm, explicitly fitting the MoS_2 monolayer emission band, is provided in Figure S7, displaying an emission spectrum with intensity enhancement primarily at quasi-BIC modes. This highlights the capability of the quasi-BIC mode of the membrane metasurface to enhance the emission characteristics of different TMDC monolayers, demonstrating its versatility in promoting light-matter interactions for diverse 2D materials.

Conclusion

In summary, we have demonstrated the effective coupling of TMDC monolayers with a finite-area metasurface utilizing quasi-BIC modes within an air-suspended membrane photonic structure. This approach has led to significantly enhanced light-matter interactions and spontaneous emission from the TMDC monolayers. By employing the membrane metasurface, the out-of-plane symmetry is preserved, effectively minimizing radiation losses and achieving strong field enhancement through quasi-BIC modes. Consequently, the high-Q emission extends over an area of several micrometers, markedly different from the emission characteristics of photonic crystal cavities and plasmonic nanostructures. This highlights the superiority of utilizing quasi-BIC modes on membrane metasurfaces for coupling with 2D layered materials, demonstrating their potential for advanced quantum and nanophotonic applications.

Methods

2D Material Dry Transfer

TMDC (WSe_2 and MoS_2) flakes (HQ Graphene, Netherlands) were prepared on a polydimethylsiloxane (PDMS) sheet by mechanical exfoliation of bulk crystals. The TMDC flakes were then transferred onto commercially available 90 nm-thick SiO2/Si substrates to enable the identification of the layer number via optical contrast under the optical microscope. A suitable monolayer flake was identified and then transferred onto the target SiN membrane metasurface using a homebuilt micromanipulator setup using the anthracene-assisted transfer process.[49] First, we grow the anthracene crystals by heating anthracene powder (Sigma Aldrich, USA) to ~80˚C. The sublimated anthracene vapor will then recrystallize on the bottom surface of a glass slide which is placed at ~1 mm above the anthracene powder. The growth time of the anthracene crystal is typically about 10 hours. A small PDMS sheet was then placed on a glass slide, followed by an anthracene crystal on the PDMS to form an anthracene/PDMS stamp which was then used to pick up the TMDC flake. The TMDC flake and the anthracene crystal were then transferred together onto the target membrane metasurface provided by Ted Pella, Inc., USA. Finally, the anthracene crystal was heated to ~80˚C or left in ambient conditions to sublime, leaving behind the TMDC flake with a clean interface.

Simulation

The far-field reflectance spectra and dispersion diagram of the membrane metasurfaces, as well as the near-field electric and magnetic field distributions of the resonance modes, were computed using the rigorous coupled-wave analysis (DiffractMOD, RSoft Design Group, USA) and the finite-difference time-domain technique (FullWAVE, RSoft Design Group, USA). All simulations were performed under periodic boundary conditions in the x- and y-axes and perfectly matched-layer conditions in the z-axis, with plane-wave light incidence and the incident angle along the z-axis. The electric field **E** is normalized by the electric field amplitude of the incident light. The electric energy density is defined as $U_E = ½\int \mathrm{Re}[\varepsilon(\mathbf{r}')]|\mathbf{E}|^2\, dV$, where **E** is the electric field, ε is the spatially dependent permittivity, and V is the volume of the simulation grid. The simulation of the finite-area membrane metasurface was performed using a finite-size domain with $N = 31$, where N represents the number of air holes along the x direction. The non-structured region surrounding the metasurface measures 3 μm, and the boundary conditions in the x, y, and z directions are modeled using perfectly matched layers (PMLs). The simulation was conducted for the resonances at $\theta_y = \pm 2^\circ$ to show the symmetric distribution.

Optical Measurement

The experimental optical properties of the SiN membrane metasurfaces and the WSe_2- and MoS_2-coupled membrane metasurfaces were obtained utilizing a confocal laser microscope system (alpha300 R, WITec (Oxford Instruments Group), Germany). The samples were excited with a CW laser at 488 nm. The excitation light and the emission light were focused and collected, respectively, by objective lenses with magnifications of 10x (NA = 0.25, corresponding to an angle within 14.48˚ in air) and 20x (NA = 0.45, corresponding to an angle within 14.48˚ in air). The excited emission was collected and analyzed with a spectrometer. The emission intensity distributions were obtained using a motorized x-y-sample scanning stage for confocal emission imaging.

FIGURES

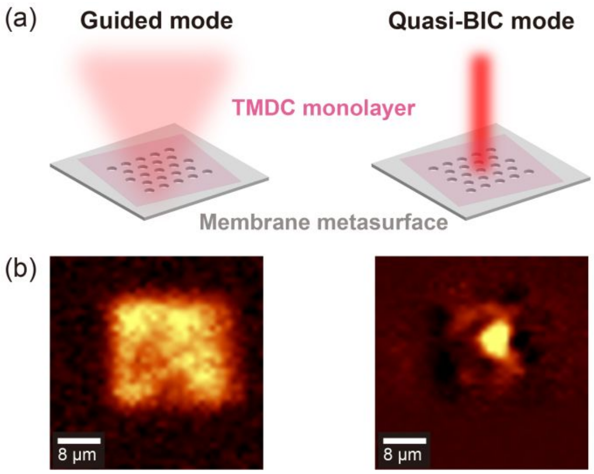

Figure 1. Membrane metasurfaces featuring finite-area dimensions supporting TMDC-monolayer-coupled quasi-BIC surface emission. a) Schematic diagrams and b) emission intensity distributions of WSe_2 monolayers coupled to a finite-area membrane metasurface for supporting optical guided mode and quasi-BIC mode surface emission. The metasurface area is 25 μm × 25 μm. The scale bars are 8 μm.

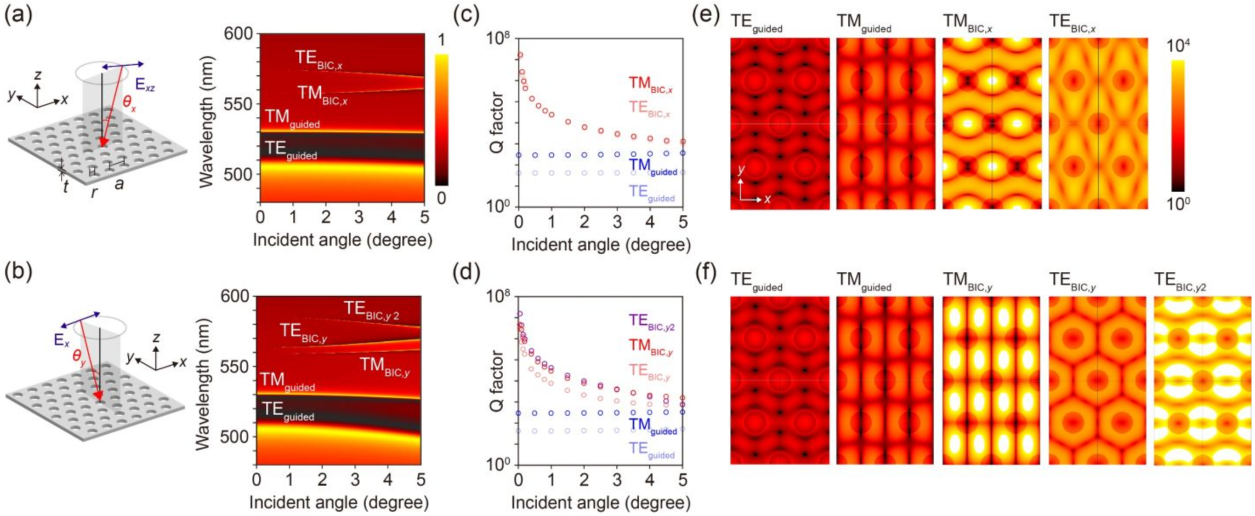

Figure 2. Design and characterization of guided and quasi-BIC modes based on the membrane metasurface. a) and b) Simulated reflection spectral variation to the light incident angle along the *x* and *y* axes. The membrane metasurface consists of a triangular lattice of airholes with lattice period $a = 400$ nm and radius $r = 90$ nm in a SiN slab of thickness $t = 205$ nm. The schematics illustrate the light incident angle and polarization. The scale bar is shared between a and b. c) and d) Simulated Q-factor variation to the incident angle of guided modes and quasi-BIC modes. e) and f) Electric energy density distributions of the guided and quasi-BIC modes indicated in a. The distributions are provided in the *xy* plane in the middle of the membrane. The scale bar is in logarithmic scale and shared between e and f.

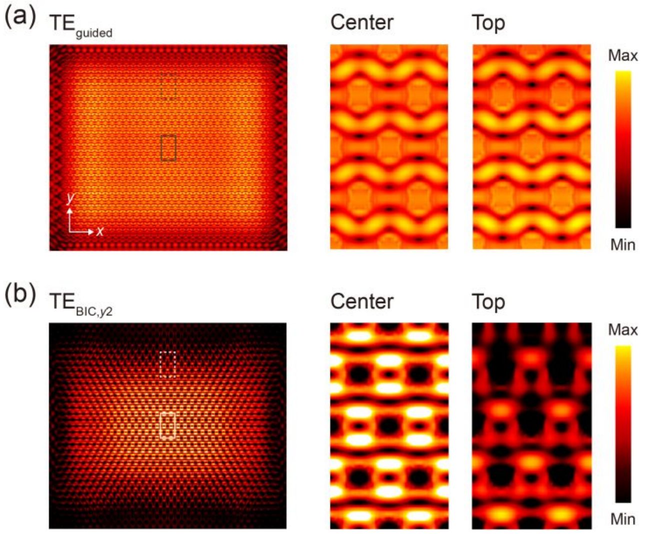

Figure 3. Simulations of the guided mode and quasi-BIC mode based on the finite-area membrane metasurface. Electric energy density distributions of a) the guided mode ($\mathrm{TE}_{\mathrm{guided}}$) and b) the quasi-BIC mode ($\mathrm{TE}_{\mathrm{BIC},y2}$) indicated in Figure 2b. The distributions are provided in the *xy* plane in the middle of the membrane. The scale bars are in logarithmic scales.

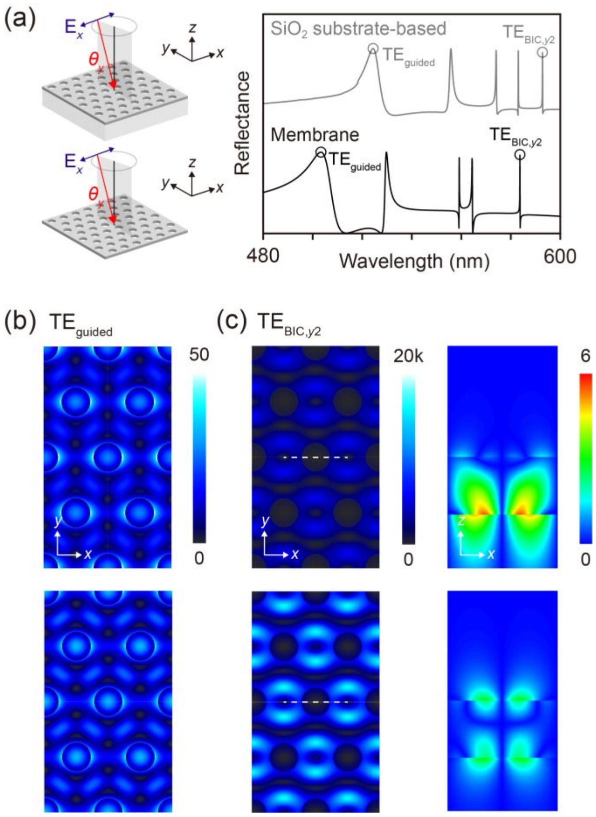

Figure 4. Comparison of the guided mode and quasi-BIC mode in the membrane metasurface and substrate-based metasurface. (a) Simulated reflectance spectra of the membrane metasurface (black) and the metasurface on the top of the SiO_2 substrate (gray). (b) Electric energy density distribution of the guided mode (TE_{guided}) in the membrane metasurface (top) and substrate-based metasurface (bottom). (c) Electric energy density distributions (left) and electric field distributions in the *z*-direction (E_z) (right) of the quasi-BIC mode ($TE_{BIC,y2}$) in the membrane metasurface (top) and substrate-based metasurface (bottom). The E_z distributions are demonstrated in the *xz* plane, as indicated by the white dashed lines.

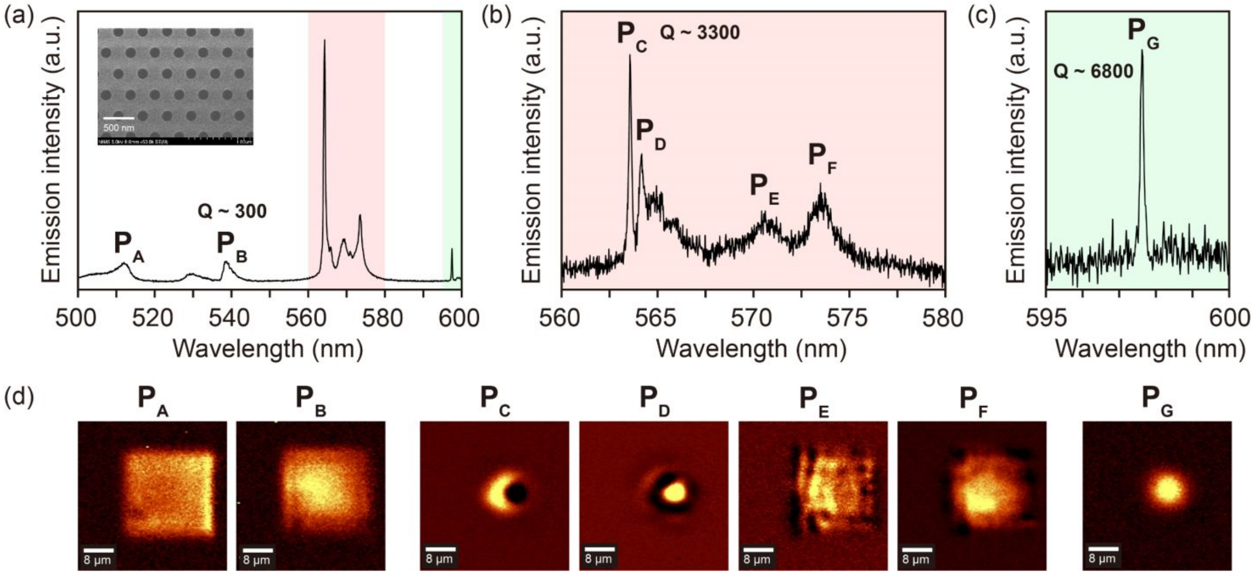

Figure 5. Spontaneous emission behaviors of the finite-area SiN membrane metasurface. a) Spontaneous emission spectra of the membrane metasurface. The SEM image of the measured membrane metasurface is provided as the inset. The scale bar is 500 nm. b) and c) The details of the regions highlighted in light red and light green in Figure 5a. d) Emission intensity distributions of the guided modes and quasi-BIC modes indicated from P_A to P_G in a. The scale bars are 8 μm.

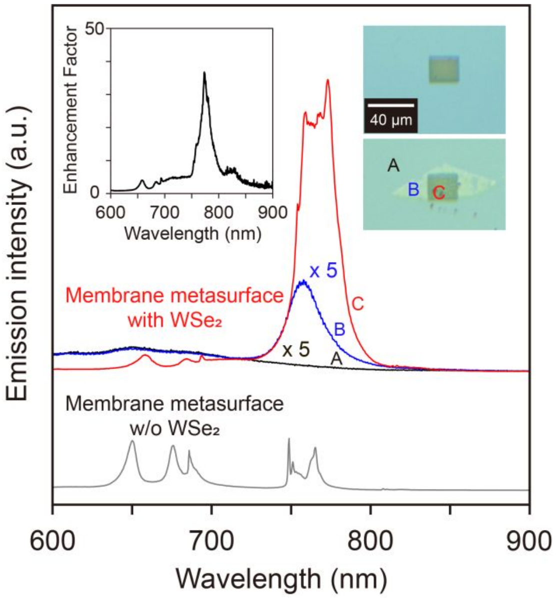

Figure 6. Coupling of the TMDC monolayer to the membrane metasurface via quasi-BIC mode. Spontaneous emission spectra of the SiN membrane (black), WSe_2 monolayer on the membrane (blue), SiN membrane metasurface with a period of 600 nm (gray), and WSe_2 monolayer coupled to the membrane metasurface (red). The insets display the enhancement factor between the emission from the WSe_2 monolayer on the membrane metasurface and the WSe_2 monolayer on the membrane, along with optical microscope images of the membrane metasurface with and without the WSe_2 monolayer on top. The scale bar is 40 μm. The excitation power for the measurements is 5 mW.

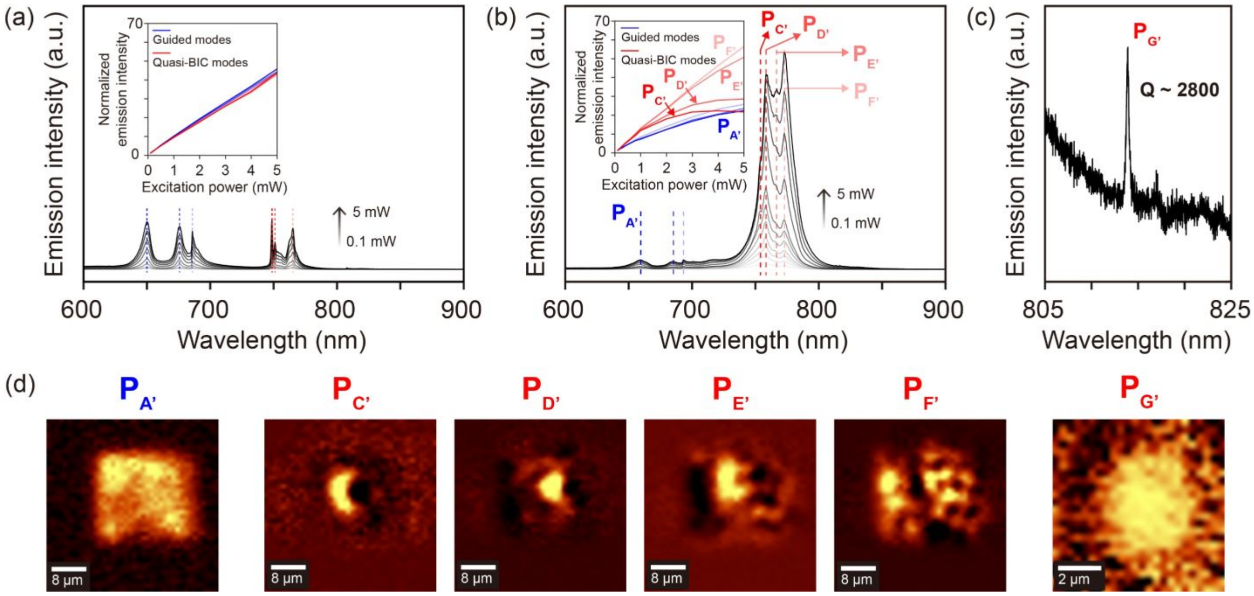

Figure 7. Emission behaviors of the TMDC monolayer coupled to the membrane metasurface. a) Variation in the spontaneous emission spectrum of the SiN membrane metasurface and b) WSe_2 monolayer coupled to the membrane metasurface as a function of excitation power from 0.1 mW to 5 mW. The insets show the intensity ratio normalized to the intensity at 0.1 mW at the wavelengths indicated in a and b. c) Detailed spontaneous emission spectrum of the WSe_2 coupled to the membrane metasurface at 805–825 nm. d) Emission intensity mapping of the WSe_2 monolayer coupled to the membrane metasurface at the wavelength indicated in d. The scale bars are 8 μm for $P_{A'}$ to $P_{F'}$ and 2 μm for $P_{G'}$.

ToC graphic

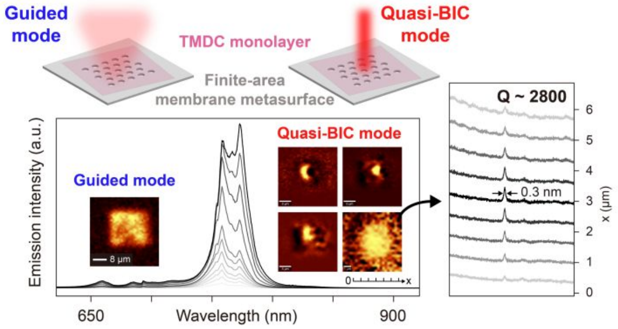

ASSOCIATED CONTENT

Supporting Information

The Supporting Information is available free of charge at

Detailed design, mode analysis, and characterization of the membrane metasurfaces; SEM images of the membrane metasurface samples; supplementary experimental results and analysis on spontaneous emission from WSe_2 and MoS_2 monolayers coupled to the membrane metasurfaces (PDF)

AUTHOR INFORMATION

Corresponding Author

* E-mail: HO.Ya-Lun@nims.go.jp

Author Contributions

The manuscript was written through the contributions of all authors. All authors have given approval to the final version of the manuscript.

ACKNOWLEDGMENT

This work was supported by JSPS KAKENHI Grant Numbers JP23K26155, JP23H01461, JP23H00253, JP21H04660, JP22K14623, JP23H00262, JP24K17627. A part of this work was supported by "Advanced Research Infrastructure for Materials and Nanotechnology in Japan (ARIM)" of the Ministry of Education, Culture, Sports, Science and Technology (MEXT) (Proposal Number JPMXP1223NM5440) and RIKEN Incentive Research Projects. Financial support by the Center of Atomic Initiative for New Materials (AI-Mat), National Taiwan University, from the Featured Areas Research Center Program within the framework of the Higher Education Sprout Project by the Ministry of Education in Taiwan (Grant No. 108L9008), is also acknowledged. C.F.F. is supported by the RIKEN SPDR fellowship. Y.L.H. would like to extend grateful appreciation to Dr. Hideki Miyazaki and Dr. Masanobu Iwanaga from the Research Center for Electronic and Optical Materials, NIMS, for their important discussions and technical support.

REFERENCES

1. Xia, F. N.; Wang, H.; Xiao, D.; Dubey, M.; Ramasubramaniam, A., Two-dimensional material nanophotonics. *Nature Photonics* **2014,** *8* (12), 899-907.

2. Turunen, M.; Brotons-Gisbert, M.; Dai, Y. Y.; Wang, Y. D.; Scerri, E.; Bonato, C.; Jöns, K. D.; Sun, Z. P.; Gerardot, B. D., Quantum photonics with layered 2D materials. *Nature Reviews Physics* **2022,** *4* (4), 219-236.

3. Mak, K. F.; Lee, C.; Hone, J.; Shan, J.; Heinz, T. F., Atomically thin MoS(2): a new direct-gap semiconductor. *Phys Rev Lett* **2010,** *105* (13), 136805.

4. Splendiani, A.; Sun, L.; Zhang, Y.; Li, T.; Kim, J.; Chim, C. Y.; Galli, G.; Wang, F., Emerging photoluminescence in monolayer MoS2. *Nano Lett* **2010,** *10* (4), 1271-5.

5. Mak, K. F.; Shan, J., Photonics and optoelectronics of 2D semiconductor transition metal dichalcogenides. *Nature Photonics* **2016,** *10* (4), 216-226.

6. Mueller, T.; Malic, E., Exciton physics and device application of two-dimensional transition metal dichalcogenide semiconductors. *Npj 2d Materials and Applications* **2018,** *2* (1).

7. Raja, A.; Chaves, A.; Yu, J.; Arefe, G.; Hill, H. M.; Rigosi, A. F.; Berkelbach, T. C.; Nagler, P.; Schuller, C.; Korn, T.; Nuckolls, C.; Hone, J.; Brus, L. E.; Heinz, T. F.; Reichman, D. R.; Chernikov, A., Coulomb engineering of the bandgap and excitons in two-dimensional materials. *Nat Commun* **2017,** *8*, 15251.

8. Wang, G.; Chernikov, A.; Glazov, M. M.; Heinz, T. F.; Marie, X.; Amand, T.; Urbaszek, B., Excitons in atomically thin transition metal dichalcogenides. *Rev Mod Phys* **2018,** *90* (2).

9. Anantharaman, S. B.; Jo, K.; Jariwala, D., Exciton-Photonics: From Fundamental Science to Applications. *ACS Nano* **2021,** *15* (8), 12628-12654.

10. Huang, L.; Krasnok, A.; Alu, A.; Yu, Y.; Neshev, D.; Miroshnichenko, A. E., Enhanced light-matter interaction in two-dimensional transition metal dichalcogenides. *Rep Prog Phys* **2022,** *85* (4).

11. Wu, S.; Buckley, S.; Schaibley, J. R.; Feng, L.; Yan, J.; Mandrus, D. G.; Hatami, F.; Yao, W.; Vuckovic, J.; Majumdar, A.; Xu, X., Monolayer semiconductor nanocavity lasers with ultralow thresholds. *Nature* **2015,** *520* (7545), 69-72.

12. Fryett, T. K.; Seyler, K. L.; Zheng, J.; Liu, C.-H.; Xu, X.; Majumdar, A., Silicon photonic crystal cavity enhanced second-harmonic generation from monolayer WSe2. *2D Materials* **2016,** *4* (1).

13. Zhang, L.; Gogna, R.; Burg, W.; Tutuc, E.; Deng, H., Photonic-crystal exciton-polaritons in monolayer semiconductors. *Nat Commun* **2018,** *9* (1), 713.

14. Sortino, L.; Zotev, P. G.; Mignuzzi, S.; Cambiasso, J.; Schmidt, D.; Genco, A.; Assmann, M.; Bayer, M.; Maier, S. A.; Sapienza, R.; Tartakovskii, A. I., Enhanced light-matter interaction in an atomically thin semiconductor coupled with dielectric nano-antennas. *Nat Commun* **2019,** *10* (1), 5119.

15. Ma, X.; Youngblood, N.; Liu, X.; Cheng, Y.; Cunha, P.; Kudtarkar, K.; Wang, X.; Lan, S., Engineering photonic environments for two-dimensional materials. *Nanophotonics* **2021,** *10* (3), 1031-1058.

16. Iwanaga, M.; Yang, X.; Karanikolas, V.; Kuroda, T.; Sakuma, Y. Prominently Enhanced Luminescence from a Continuous Monolayer of Transition Metal Dichalcogenide on All-Dielectric Metasurfaces. *Nanophotonics* **2024**, *13*, 95-105

17. Marinica, D. C.; Borisov, A. G.; Shabanov, S. V., Bound States in the continuum in photonics. *Phys Rev Lett* **2008,** *100* (18), 183902.

18. Yang, Y.; Peng, C.; Liang, Y.; Li, Z.; Noda, S., Analytical perspective for bound states in the continuum in photonic crystal slabs. *Phys Rev Lett* **2014,** *113* (3), 037401.

19. Hsu, C. W.; Zhen, B.; Stone, A. D.; Joannopoulos, J. D.; Soljačić, M., Bound states in the continuum. *Nature Reviews Materials* **2016,** *1* (9).

20. Doeleman, H. M.; Monticone, F.; den Hollander, W.; Alù, A.; Koenderink, A. F., Experimental observation of a polarization vortex at an optical bound state in the continuum. *Nature Photonics* **2018,** *12* (7), 397-401.

21. Yang, J. H.; Huang, Z. T.; Maksimov, D. N.; Pankin, P. S.; Timofeev, I. V.; Hong, K. B.; Li, H.; Chen, J. W.; Hsu, C. Y.; Liu, Y. Y.; Lu, T. C.; Lin, T. R.; Yang, C. S.; Chen, K. P., Low‐Threshold Bound State in the Continuum Lasers in Hybrid Lattice Resonance Metasurfaces. *Laser & Photonics Reviews* **2021,** *15* (10).

22. Hwang, M. S.; Lee, H. C.; Kim, K. H.; Jeong, K. Y.; Kwon, S. H.; Koshelev, K.; Park, H. G. Ultralow-threshold laser using super-bound states in the continuum. Nat. Commun. 2021, 12 (1), 4135.

23. Zhong, H.; Yu, Y.; Zheng, Z.; Ding, Z.; Zhao, X.; Yang, J.; Wei, Y.; Chen, Y.; Yu, S., Ultra-low threshold continuous-wave quantum dot mini-BIC lasers. *Light Sci Appl* **2023,** *12* (1), 100.

24. Liu, C. C.; Hsiao, H. H.; Chang, Y. C., Nonlinear two-photon pumped vortex lasing based on quasi-bound states in the continuum from perovskite metasurface. *Sci Adv* **2023,** *9* (22), eadf6649.

25. Richter, F. U.; Sinev, I.; Zhou, S.; Leitis, A.; Oh, S. H.; Tseng, M. L.; Kivshar, Y.; Altug, H., Gradient High-Q Dielectric Metasurfaces for Broadband Sensing and Control of Vibrational Light-Matter Coupling. *Adv Mater* **2024**, e2314279.

26. Xing, D.; Chen, M. H.; Wang, Z.; Deng, C. Z.; Ho, Y. L.; Lin, B. W.; Lin, C. C.; Chen, C. W.; Delaunay, J. J., Solution‐Processed Perovskite Quantum Dot Quasi‐BIC Laser from Miniaturized Low‐Lateral‐Loss Cavity. *Advanced Functional Materials* **2024**.

27. Ge, X.; Minkov, M.; Fan, S.; Li, X.; Zhou, W., Laterally confined photonic crystal surface emitting laser incorporating monolayer tungsten disulfide. *npj 2D Materials and Applications* **2019,** *3* (1).

28. Kravtsov, V.; Khestanova, E.; Benimetskiy, F. A.; Ivanova, T.; Samusev, A. K.; Sinev, I. S.; Pidgayko, D.; Mozharov, A. M.; Mukhin, I. S.; Lozhkin, M. S.; Kapitonov, Y. V.; Brichkin, A. S.; Kulakovskii, V. D.; Shelykh, I. A.; Tartakovskii, A. I.; Walker, P. M.; Skolnick, M. S.; Krizhanovskii, D. N.; Iorsh, I. V., Nonlinear polaritons in a monolayer semiconductor coupled to optical bound states in the continuum. *Light Sci Appl* **2020,** *9*, 56.

29. Weber, T.; Kuhner, L.; Sortino, L.; Ben Mhenni, A.; Wilson, N. P.; Kuhne, J.; Finley, J. J.; Maier, S. A.; Tittl, A., Intrinsic strong light-matter coupling with self-hybridized bound states in the continuum in van der Waals metasurfaces. *Nat Mater* **2023,** *22* (8), 970-976.

30. Maggiolini, E.; Polimeno, L.; Todisco, F.; Di Renzo, A.; Han, B.; De Giorgi, M.; Ardizzone, V.; Schneider, C.; Mastria, R.; Cannavale, A.; Pugliese, M.; De Marco, L.; Rizzo, A.; Maiorano, V.; Gigli, G.; Gerace, D.; Sanvitto, D.; Ballarini, D., Strongly enhanced light-matter coupling of monolayer WS(2) from a bound state in the continuum. *Nat Mater* **2023,** *22* (8), 964-969.

31. Bernhardt, N.; Koshelev, K.; White, S. J. U.; Meng, K. W. C.; Froch, J. E.; Kim, S.; Tran, T. T.; Choi, D. Y.; Kivshar, Y.; Solntsev, A. S., Quasi-BIC Resonant Enhancement of Second-Harmonic Generation in WS(2) Monolayers. *Nano Lett* **2020,** *20* (7), 5309-5314.

32. Sadrieva, Z. F.; Sinev, I. S.; Koshelev, K. L.; Samusev, A.; Iorsh, I. V.; Takayama, O.; Malureanu, R.; Bogdanov, A. A.; Lavrinenko, A. V., Transition from Optical Bound States in the Continuum to Leaky Resonances: Role of Substrate and Roughness. *ACS Photonics* **2017,** *4* (4), 723-727.

33. Huang, L.; Li, S.; Zhou, C.; Zhong, H.; You, S.; Li, L.; Cheng, Y.; Miroshnichenko, A. E., Realizing Ultrahigh-Q Resonances Through Harnessing Symmetry-Protected Bound States in the Continuum. *Advanced Functional Materials* **2023,** *34* (11).

34. Kodigala, A.; Lepetit, T.; Gu, Q.; Bahari, B.; Fainman, Y.; Kante, B., Lasing action from photonic bound states in continuum. *Nature* **2017,** *541* (7636), 196-199.

35. Leitis, A.; Tseng, M.-L.; John-Herpin, A.; Kivshar, Y. S.; Altug, H. Wafer-Scale Functional Metasurfaces for Mid-Infrared Photonics and Biosensing. *Adv. Mater.* **2021**, *33*, 2102232.

36. Contractor, R.; Noh, W.; Redjem, W.; Qarony, W.; Martin, E.; Dhuey, S.; Schwartzberg, A.; Kante, B., Scalable single-mode surface-emitting laser via open-Dirac singularities. *Nature* **2022,** *608* (7924), 692-698.

37. Ren, Y.; Li, P.; Liu, Z.; Chen, Z.; Chen, Y. L.; Peng, C.; Liu, J., Low-threshold nanolasers based on miniaturized bound states in the continuum. *Sci Adv* **2022,** *8* (51), eade8817.

38. Kang, M.; Zhang, Z.; Wu, T.; Zhang, X.; Xu, Q.; Krasnok, A.; Han, J.; Alu, A., Coherent full polarization control based on bound states in the continuum. *Nat Commun* **2022,** *13* (1), 4536.

39. Ma, X.; Kudtarkar, K.; Chen, Y.; Cunha, P.; Ma, Y.; Watanabe, K.; Taniguchi, T.; Qian, X.; Hipwell, M. C.; Wong, Z. J.; Lan, S., Coherent momentum control of forbidden excitons. *Nat Commun* **2022,** *13* (1), 6916.

40. Wu, S.; Buckley, S.; Jones, A. M.; Ross, J. S.; Ghimire, N. J.; Yan, J.; Mandrus, D. G.; Yao, W.; Hatami, F.; Vučković, J.; Majumdar, A.; Xu, X. Control of Two-Dimensional Excitonic Light Emission via Photonic Crystal. *2D Mater.* **2014**, *1*, 011001.

41. Li, Y.; Zhang, J.; Huang, D.; Sun, H.; Fan, F.; Feng, J.; Ning, C. Z. Room-Temperature Continuous-Wave Lasing from Monolayer Molybdenum Ditelluride Integrated with a Silicon Nanobeam Cavity. *Nat. Nanotechnol.* **2017**, *12*, 987-992

42. Liu, Y.; Fang, H.; Rasmita, A.; Zhou, Y.; Li, J.; Yu, T.; Gao, W. Room-Temperature Nanocavity Laser with Interlayer Excitons in 2D Heterostructures. *Sci. Adv.* **2019**, *5*, eaav4506

43. Paik, E. Y.; Zhang, L.; Burg, G. W.; Gogna, R.; Tutuc, E.; Deng, H. Interlayer Exciton Laser of Extended Spatial Coherence in Atomically Thin Heterostructures. *Nature* **2019**, *576*, 80-84.

44. Butun, S.; Tongay, S.; Aydin, K. Enhanced Light Emission from Large-Area Monolayer MoS2 Using Plasmonic Nanodisc Arrays. *Nano Lett.* **2015**, *15*, 2700-2704

45. Wang, Z.; Dong, Z.; Gu, Y.; Chang, Y.-H.; Zhang, L.; Li, L.-J.; Zhao, W.; Eda, G.; Zhang, W.; Grinblat, G.; Maier, S. A.; Yang, J. K. W.; Qiu, C.-W.; Wee, A. T. S. Giant Photoluminescence Enhancement in Tungsten-Diselenide-Gold Plasmonic Hybrid Structures. *Nat. Commun.* **2016**, *7*, 11283

46. Sun, K.; Wang, W.; Han, Z. High-Q Resonances in Periodic Photonic Structures. Phys. Rev. B 2024, 109 (8), 085426.

47. Hoang, T. X.; Leykam, D.; Kivshar, Y. Photonic Flatband Resonances in Multiple Light Scattering. Phys. Rev. Lett. **2024**, *132* (4), 043803.

48. Mouri, S.; Miyauchi, Y.; Toh, M.; Zhao, W.; Eda, G.; Matsuda, K. Nonlinear Photoluminescence in Atomically Thin Layered WSe_2 Arising from Diffusion-Assisted Exciton-Exciton Annihilation. Phys. Rev. B 2014, 90 (15), 155449.

49. Otsuka, K.; Fang, N.; Yamashita, D.; Taniguchi, T.; Watanabe, K.; Kato, Y. K., Deterministic transfer of optical-quality carbon nanotubes for atomically defined technology. *Nat Commun* **2021,** *12* (1), 3138.